Engineering Fracture Mechanics 326 (2025) 111318

Contents lists available at ScienceDirect

Engineering Fracture Mechanics

journal homepage: www.elsevier.com/locate/engfracmech

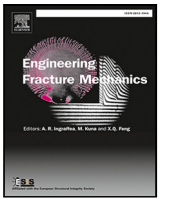

Rotation control with dual actuators: A new device to extract mixed-mode traction–separation relations

Mohammad A. Ansari [a], Rujing Zha [b], Rui Huang [a], Kenneth M. Liechti [a,*]

[a] Department of Aerospace Engineering and Engineering Mechanics, University of Texas, Austin, TX, 78712, USA
[b] Department of Mechanical Engineering, Northwestern University, Northwestern University, Evanston, IL, 60208, USA

ARTICLE INFO

Keywords:
Traction–separation relation
Mixed mode
Dual actuator
Rotation control
Interfacial fracture

ABSTRACT

This paper addresses the extraction of traction-separation relations associated with the mixed-mode interactions at the interfaces between two materials in the context of cohesive zone modeling for large scale bridging during delamination. A direct approach that provides the normal and shear components of the traction-separation relation at any mode-mix is pursued using a novel rotation-controlled loading device. In the past, multiple laminated beam specimen geometries have been used to vary the mode-mix. However, when using the same specimen geometry is desirable, dual actuation provides the most general solution to mixed-mode loading path control. Based on our previous work, rotation control of laminated beams has been proposed as being optimal from crack growth stability and mode-mix control standpoints. This paper describes the implementation of this concept using laminated beams consisting of an epoxy sandwiched between aluminum strips. Digital image correlation was used to determine the location of the crack front and measure the normal and shear components of the crack tip separations. The specimen geometry allows the normal and shear components of the J-integral to be determined separately via measurements of the reactive torques. The normal and shear components of the traction–separation relations for five different mode-mixes are then presented. The results challenge some of the commonly accepted trends regarding the initiation and evolution of damage. The change of mode-mix as the damage evolves is also discussed as it relies heavily on the definition of the mode-mix.

1. Introduction

Cohesive zone modeling, introduced in [1,2] has emerged as an improvement over linear elastic fracture mechanics through its usage of multiple parameters to define the fracture process [3,4]. All the local near tip inelastic phenomena can be bundled together to provide an effective traction-separation relation across the crack faces. The generality of this approach has led to its wide range of applications, including the descriptions of atomic forces [5], polymer crazing [6], damage of fiber reinforced composites [7] and crack nucleation from corners [8,9]. However, such a modeling approach is limited by the accuracy of the input traction-separation relations. Extracting the traction-separation relations is challenging in mixed-mode cases as the normal and shear interactions are generally coupled and mode-mix dependent.

There are a number of approaches for extraction of traction-separation relations [10]. First, the direct approach utilizes the measurements of the J-integrals and crack tip openings to determine the traction-separation relations using analytical expressions in terms of the crack length and actuator displacements or reaction forces [11,12]. Secondly, numerical simulations may be performed

* Corresponding author.
E-mail address: kml@mail.utexas.edu (K.M. Liechti).

https://doi.org/10.1016/j.engfracmech.2025.111318
Received 22 April 2025; Received in revised form 27 May 2025; Accepted 31 May 2025
Available online 16 June 2025

Nomenclature

δ_n, δ_t	Normal and tangential separation along the crack faces
δ_n^*, δ_t^*	Normal and tangential crack tip separations
δ_n^f, δ_t^f	Range of normal and tangential interactions
δ_n^i, δ_t^i	Normal and shear separations at damage initiation
Γ	Total fracture toughness
Γ_0, λ	Fitting parameters
Γ_1, Γ_2	Individual components of fracture toughness
λ_n	$\left(\frac{6k_n}{Eh^3}\right)^{0.25}$
$\mathcal{M}_1, \mathcal{M}_2$	Reactive end moments
ϕ_1, ϕ_2	Local rotations of the neutral axes
ψ	Generic mode-mix
ψ_J, ψ_δ	Global and local measures of mode-mix
σ, τ	Normal and shear tractions along the interface
σ_0, τ_0	Normal and shear strengths of the interface
Θ_1, Θ_2	Applied end rotations
Θ_d, Θ_s	$\left(\frac{\Theta_1-\Theta_2}{2}\right), \left(\frac{\Theta_1+\Theta_2}{2}\right)$
$\tilde{x}$	Coordinate internal to the digital image correlationsoftware
a	Crack length
b	Width of the beam
D	Generic damage parameter
D_n, D_t	Normal and shear damage parameters
E, ν	Young's modulus and Poisson's ratio
h	Thickness of the beam
J_1, J_2	Individual components of the J-integral
k_n, k_t	Normal and shear stiffnesses of the interface
L	Total length of the specimen
M_d, M_s	$\left(\frac{\mathcal{M}_1-\mathcal{M}_2}{2}\right), \left(\frac{\mathcal{M}_1+\mathcal{M}_2}{2}\right)$
u_1, u_2	Axial displacements of the neutral axes
v_1, v_2	Transverse displacements of the neutral axes
x	Coordinate along the length of the specimen

iteratively while varying the parameters of the traction-separation relations to minimize the error between the simulated readings and the experimental results until convergence is reached [13,14]. The iterative method thus requires fewer experimental results, but suffers in that the form of the traction-separation relations must be typically be pre-determined (say bilinear, exponential, etc.) to ensure convergence. Field projection methods are a powerful class of traction-separation relation extraction approaches that are not tied to any particular form [15–19]. In the extraction process, far-field displacement data, in conjunction with auxiliary probe fields are incorporated in an interaction J-integral. Alternatively, it has been shown that, under mode I conditions, an integrated digital image correlation [20] approach, where the unknown degrees of freedom are no longer displacements or rotations, but the set of interfacial fracture properties that describe the traction-separation relations, may be used. A more recent, but related category is the use of machine learning in the extraction approach [21,22]. In this paper, we will focus on the direct approach.

From a computational perspective, traction-separation relation are often categorized as being intrinsic or extrinsic [23,24]. The former have an initial region where the tractions increase before reaching a maximum value, or the strength. After this, the cohesive tractions monotonically decrease as damage develops and become zero at a separation value that corresponds to the range of the interaction. The total area under this closed traction–separation curve is the toughness of the interface. In finite element schemes, this means that the entire traction–separation response of a particular material point has to be tracked in a simulation. On the other hand, extrinsic traction-separation relation are initially rigid, i.e., the two sides of the interface are assumed to be perfectly connected until the onset of damage. Extrinsic traction-separation relationsare therefore less physical, but offer computational efficiency as the damaging elements are only introduced once the strength has been exceeded. The direct approach mathematically yields intrinsic traction-separation relations, as opposed to extrinsic traction-separation relations.

One of the most common geometries to extract traction-separation relations, both iteratively and directly, is the laminated beam, although other approaches have been used [25,26]. Mode-mix can be induced in such laminated beams through asymmetry in geometry, materials, or loading. End notched flexure [27], mixed-mode bending [28–30], and double cantilever beam [31–33] are some configurations that have used mismatches in geometry and materials. Uneven loads have been applied via single actuator

loading configurations [11,34]. These provide nominally radial mixed-mode loading paths, while dual actuator systems [31–33] provide more general ones by simply changing the ratio of applied loads on each actuator in order to access the full range of mode-mixes on a single specimen geometry. Loads may be applied via force, displacement, rotation, or torque control, but the end displacement case is the easiest to implement and has been used in previous works.

The ease of implementing end displacements comes with complications that arise in extracting traction–separation relationships. Even though one can prescribe a constant far-field loading ratio, it often leads to non-constant and non-uniform mode-mix in the cohesive zone as the damage evolves [31], potentially invalidating the extraction process. This effect is magnified when the cohesive zone is large, since the traction-separation relation for the normal and shear interactions are coupled and in this case, one cannot confidently predict the expected mode-mix. This observation led to an analytical/numerical study exploring alternative loading conditions [35] where a simple beam on an elastic foundation model was used to model the development of cohesive zones in laminated beams under different dual actuator control configurations. Although no damage was considered analytically, it was found that loading by rotation control was superior to displacement control in several ways:

- The mode-mix in rotation-controlled loading was less sensitive to the crack length. This means that along the interface, the mode-mix is closer to being constant.
- The mode-mix is less sensitive to the ratio of rotations. Dual actuator devices depend on the loading ratio to sweep a range of mode-mix values. Less sensitivity of the mode-mix to the loading ratio means that a particular value of mode-mix can be targeted more precisely, given comparable precision in the loading mechanisms.
- The J-integral expressions are simplified where only one far field measurement (reactive moment) is sufficient to determine the J-integral (and thus the fracture toughness). For end displacement-controlled loading, at least two measurements are needed, which could include the reaction forces and far-field rotations [36] or the crack length [31].
- The J-integral does not explicitly depend on the parameters of the traction-separation relation.
- The last two points lend the self-similarity property to this loading mode [37].

These theoretical advantages of rotation control as opposed to end- applied displacement control have led to the present study. We investigate the process of extracting the traction-separation relations via a novel dual actuator rotation control device. Rotation-control devices have been tried in the past. For instance, a system capable of applying end-loading rotations to a double-cantilever beam using a complex system of wires and pulleys was designed [11]. This setup, however, cannot be easily scaled down due to its mechanical complexity and the pulleys can cause parasitic friction that may become significant when studying smaller specimens and weaker interfaces than the large fiber-reinforced beams in their work. Furthermore, the machine compliance introduced by the system of pulleys and wires make the device more prone to issues with crack growth instability in certain cases. More recently, [34] designed a rotation-controlled actuation device resembling a four-point beam in bending, with the double-cantilever beam perpendicularly connecting the two segments. This device has the advantage of simplicity of force measurement and loading – both are linear – but suffers from requiring the implementation of complex kinematics. The present device targets microelectronic packaging systems, where the length scales are relatively small. We therefore focus on laminated beam specimens close in length scale to target test coupons and structures in order to eliminate any changes of fracture properties related to size effects.

2. Methods

2.1. Theory

The direct extraction of traction-separation relations can be achieved from the knowledge of the J-integral and the local crack-tip displacements [10,12,38]. In particular, if the specimen geometry satisfies the balance condition [39], under mixed-mode conditions the normal and shear components of the J-integral, J_1 and J_2, can be determined from remote measurements. Meanwhile, if the normal and tangential components of the crack-tip separations, δ_n^* and δ_t^*, can be obtained from remote or local measurements, the traction components at the crack tip are obtained as functions of the crack-tip separations by

$$\sigma = \frac{\partial J_1}{\partial \delta_n^*} \quad \text{and} \quad \tau = \frac{\partial J_2}{\partial \delta_t^*}, \tag{1}$$

where $\sigma = \sigma(\delta_n^*, \delta_t^*)$ is the normal traction and $\tau = \tau(\delta_n^*, \delta_t^*)$ is the shear traction. Thus, such direct extraction requires simultaneous measurement of four quantities $(J_1, J_2, \delta_n^*, \delta_t^*)$. It should be noted that this direct extraction assumes that the interfacial tractions are only functions of the relative displacements across the interface, independent of the location along the interface. Of course, this assumption would be invalid in case of any heterogeneity along the interface. Even for a homogeneous interface, this assumption could be invalid if the traction–separation relation is rate dependent [40] or mode-mix dependent when the local mode-mix changes as the damage develops [35,41]. In this work, we apply loading at low rates to minimize rate effects and the end-applied rotation control carries the aforementioned advantage of minimizing the effect of crack length on mode-mix.

We note that Eq. (1) does not assume that the tractions can be derived from some (pseudo-)potential [12]. Instead, it assumes that the traction–separation relation is the same at all points along the interface. Then, by determining the J-integral along a contour enclosing the interface (first along the lower face and then the upper face), one obtains: $J = J_1 + J_2$, where $J_1 = \int \sigma d\delta_n^*$ and $J_2 = \int \tau d\delta_t^*$. The decomposition of the J-integral does not suggest that the normal and shear interactions are decoupled. In general, both J_1 and J_2 are functions of δ_n^* and δ_t^*, and both tractions are also functions of δ_n^* and δ_t^*. For example, J_2 may be understood as the work done by the shear traction. Since the shear traction depends on the normal separation, the work J_2 also depends on

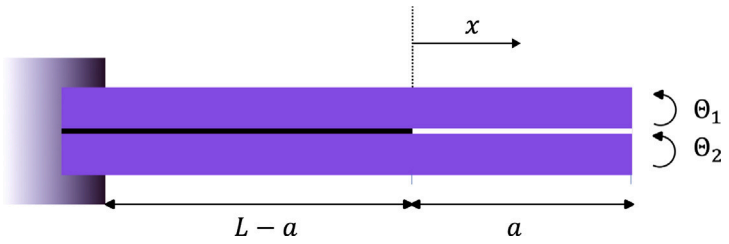

Fig. 1. Schematic of a double cantilever beam specimen loaded by end rotations.

the normal separation. Moreover, J_1, J_2 depend on the loading paths, and are not simply functions of crack tip separations as is the case with potential-based approaches.

The assumption that the traction–separation relation is the same at all points along the interface could be restrictive, especially for the case of mixed-mode fracture. Since the traction–separation relation in general depends on the mode-mix, any variation of (local) mode-mix along the interface would lead to different traction–separation relations along the interface. Even for pure Mode-I or Mode-II fracture, this assumption may not hold if the traction–separation relation is rate dependent, as shown in previous work [40]. Unloading is another case where the traction–separation relations are not the same along the interface by damage based cohesive zone models. In any case, this assumption does hold when the crack grows in a steady state, in which case every point along the interface would experience the same traction–separation history from undamaged to fully fractured. This assumption also holds when the cohesive zone model is based on a true potential.

For a symmetric, double cantilever beam under rotation control (Fig. 1), the J-integral components are decoupled as given by [35]:

$$J_1 = \frac{12M_d^2}{Eb^2h^3} \quad \text{and} \quad J_2 = \frac{9M_s^2}{Eb^2h^3}, \tag{2}$$

where E is Young's modulus, b and h are the width and thickness of the beam, respectively, $M_d = (\mathcal{M}_1 - \mathcal{M}_2)/2$ and $M_s = (\mathcal{M}_1 + \mathcal{M}_2)/2$, with $\mathcal{M}_1$ and $\mathcal{M}_2$ being the reaction moments measured at the opening ends of the specimen. If the beams are wide ($b \gg h$), we replace E by $\bar{E} = E/(1-\nu^2)$ for the plane strain case. However, for the specimen dimensions in this study ($b/h < 3$), it was determined via a finite element analysis that the plane stress condition applies. For a such a device, measurements of the reaction moments, $\mathcal{M}_1$ and $\mathcal{M}_2$, are sufficient to provide the J-integral components. This is in contrast to the displacement controlled loading, where measurements of end rotations are needed in addition to the reaction forces [36,39]. Moreover, the mode-mix in rotation-controlled loading is nearly constant along the interface [35], thus allowing a more accurate direct extraction of the traction-separation relationsunder mixed-mode conditions.

2.2. Experimental setup

The schematic and images of the developed loading device and specimen are shown in Fig. 2. We employ two separate servomotors, each with a torque carrying capacity of 0.33 Nm. The shafts of these servomotors are then attached to one end of the specimen, one on each side. Since the other end of the specimen is fixed in place, the servomotors cannot be fixed in space, as this would result in a complicated stress state in the specimen due to combined bending and axial loads. For this reason, and to ensure pure bending of the specimen, the servomotors are set to float freely on orthogonal air bearings. This means that both motors are free to move in the horizontal plane (plane of the paper in Fig. 2(a)). The specimen is symmetric and the mode-mix is introduced by controlling the gearing ratio, Θ_2/Θ_1, of the two motors. An image of the actual device appears in Fig. 2(b) along with a close-up of the specimen (Fig. 2(c))

The deformation of the specimen is monitored from the top through a camera (Basler ace U acA2440) that was combined with a Schneider XENOPLAN 2.8/50-0902 lens and a 40 mm extension tube. The sensor size was 8.45 × 7.07 mm with 2448 × 2048 pixels. The spatial calibration was 3.5 μm per pixel for a field of view of 8.5 × 7.2 mm.

The displacement resolution was determined by applying rigid body motions to an Aluminum beam and measuring the displacement along the neutral axis. The average displacement and standard deviation were determined from the data and compared with the rigid body motion that was applied to the beam. It was determined that the standard deviation in displacement, and therefore the resolution, was 0.05 μm.

The nominal frame rate of the camera is 75 fps, but the acquisition rate used in the experiments was 2 fps. This arrangement captured images in the region near the crack tip and measured the crack tip separations by digital image correlation (Fig. 2(d)), which is essential for the direct extraction of traction-separation relations. The fiducial mark establishes the approximate location of the crack front prior to analysis. Using this approach is an improvement over previous studies, in which the crack tip separations were determined indirectly based on far-field measurements [31,39].

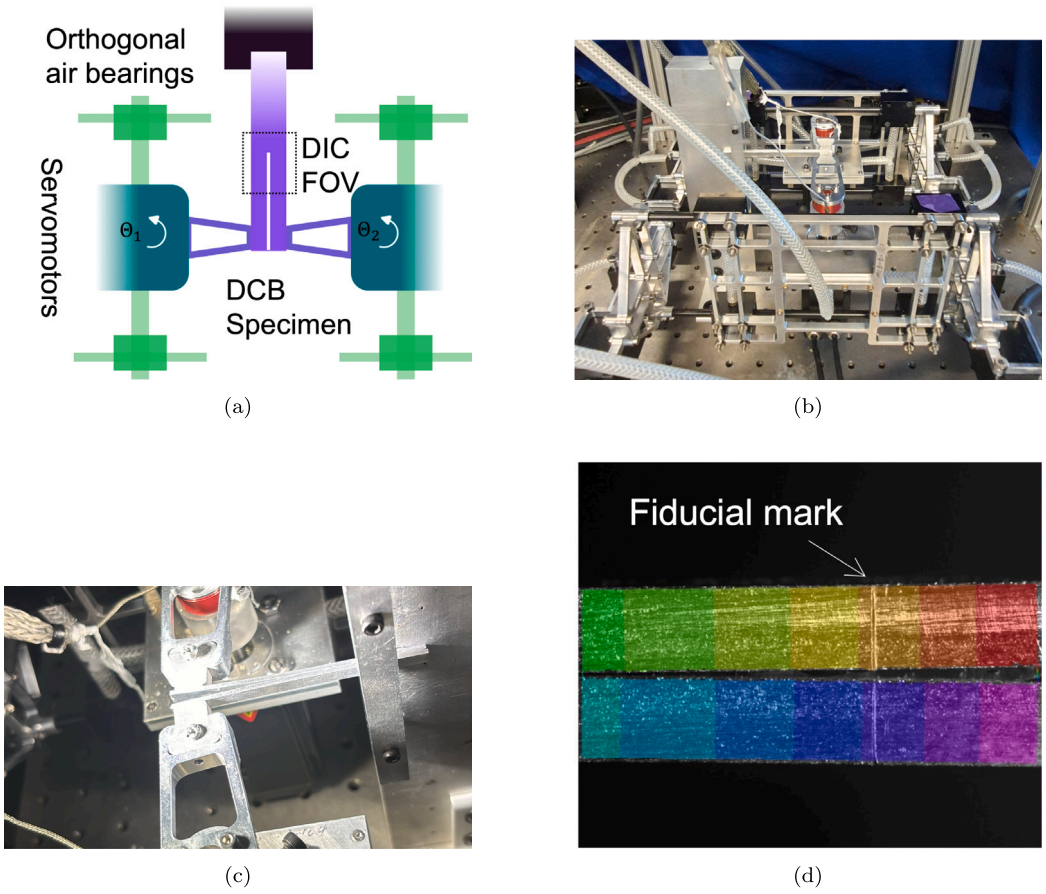

Fig. 2. A loading device for controlling end rotations on a laminated beam specimen through two servomotors. (a) Schematic of the device as viewed from the top, and (b) image of the device showing the specimen clamped on the left and attached to the motors on the right. (c) A close-up view of the specimen and (d) vertical displacement contours obtained from digital image correlation. The fiducial mark establishes the approximate location of the crack front prior to analysis.

2.3. Samples

With an eye towards using the device for measuring adhesion in microelectronics packaging, we limit ourselves to relatively small specimens and thin adhesive layers. For demonstration purposes, the adherends are nominally identical strips of hardened Aluminum 6061 (nominal yield strength of 240 MPa), of length 75 mm, width of 4.2 mm ± 0.03 mm and height of 1.59 mm ± 0.02 mm. The effective length of the specimen after clamping is 50 mm. The strips were cleaned with acetone and isopropyl alcohol before bonding. Master Bond epoxy EP30 was used to bond two adherend strips to form a laminated beam specimen. The two parts of the epoxy are mixed in a ratio of 4:1 resin:hardener by weight. Once mixed, the solution is briefly heated to 32 °C under vacuum for degassing for 20 min. The mixture is applied to the Al strips, which are then pressed together. The samples are then cured for 2 h at 100 °C before testing. Testing is performed between 2 and 10 days after curing. The epoxy thickness in the cured samples was between 15 and 40 μm. Since the epoxy layer is about two orders of magnitude thinner than the adherends, we treat it as behaving as an interface without considering the deformation of the epoxy explicitly.

3. Locating the crack tip

Specimens with opaque adherends, such as Al used in this study, produce a challenge in locating the initial crack tip. Traditionally, researchers have applied a teflon tape over a region of the adherends before curing, and used the tape to locate the initial crack tip [36,42]. The thickness of the teflon tape is typically about 100 μm, thicker than the epoxy layers in this work and therefore not suitable. Here, we use the idea of beam deformation [43] to estimate the location of the crack tip. It will be seen that this approach is more powerful for rotation control than it is for displacement control due to the self similarity property of specimens under end rotation control with respect to crack length.

Consider the specimen geometry in Fig. 1 loaded under the symmetric Mode I condition, that is, $\Theta_2/\Theta_1 = -1$. Assume the loading to be limited to such deformation that damage does not initiate at the interface, so that the normal interaction between the

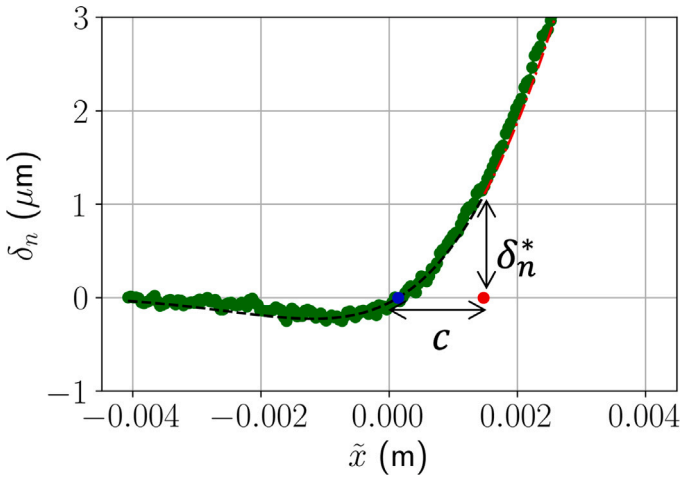

Fig. 3. Normal separation data (green dots) is fitted with Eq. (3) to determine the location of the crack tip. The blue dot marks the transition from a tensile to compressive interaction, and the red dot marks the location of the crack tip at $\tilde{x} = c$, with a normal separation δ_n^*. The two parts of Eq. (3) are shown as black dashed ($x < 0$) and red dot-dashed ($x > 0$) curves, respectively.

two beams is linear with an effective stiffness k_n and the normal traction at the interface is related to the normal separation δ_n as $\sigma = k_n\delta_n$. Such a Winkler foundation approach has been used to develop analytical expressions for cohesive zone models [35,44,45]. Assuming linearly elastic deformation for the adherend beams, the normal separation across the interface along the length of the specimen is given as [35]

$$\delta_n(x) = \begin{cases} \dfrac{12M_d}{Ebh^3\lambda_n^2}\exp(\lambda_n x)\left(\sin(\lambda_n x) + \cos(\lambda_n x)\right), & x \in (-(L-a), 0), \\ \dfrac{12M_d}{Ebh^3}\left(x + \lambda_n^{-1}\right)^2, & x \in (0, a). \end{cases} \tag{3}$$

where $\lambda_n = \left(\frac{6k_n}{Eh^3}\right)^{1/4}$ and $x = 0$ at the crack tip. In this case, the moment M_d is linearly proportional to the applied end rotation, $\Theta_d = (\Theta_1 - \Theta_2)/2$. Thus, rotation control is equivalent to moment control prior to damage initiation. Eq. (3) predicts that, under rotation or moment control, the opening profile of the interface is self-similar in Mode I, independent of the crack length a. In contrast, the analogous opening profile under displacement or force control does depend on the crack length and thus is not self-similar, even for Mode I [35].

Based on Eq. (3), the location of the initial crack tip can be determined using the following approach:

- Drive a small wedge from one end of the specimen, developing a sharp crack tip. A C-clamp is applied prior to inserting the wedge, so that the crack tip is located near the clamped region and marked with the fiducial line shown in Fig. 2(d).
- Focus the camera for digital image correlation near the estimated crack tip location.
- Load the specimen under Mode I condition by rotation control. Make sure that the applied rotation is small so that it does not initiate damage.
- Simultaneously measure the moment reactions, M_d, and displacement profiles near the crack tip by digital image correlation. The separation between the lower surface of the upper beam and the upper surface of the lower beam is then computed along the interface.
- Fit the measured separation profile, $\delta_n(\tilde{x})$, with the function $\delta_n(x)$ in Eq. (3), with $x = \tilde{x} - c$, for two parameters λ_n and c. Then, the crack tip is located at $\tilde{x} = c$.

Fig. 3 illustrates this process. Notice that the coordinate $\tilde{x}$ is the location in the digital image correlation software, which has no bearing to the x coordinate in the geometry as shown in Fig. 1. Since the location of the crack tip is unknown apriori, the parameter c accounts for a linear translation for the function $\delta_n(x)$ to align it horizontally with the measured profile $\delta_n(\tilde{x})$. The function $\delta_n(x)$ in Eq. (3) has two parts, one for the region with linear interactions ($x < 0$) and the other for the region with no interactions ($x > 0$). The region with linear interactions includes tensile interactions near the crack tip and compressive interactions further ahead of the crack tip. To fit the data for the region with linear interactions, we use the data in the range from around the minimum δ_n with compressive interactions to around the transition point with $\delta_n = 0$ (the blue dot in Fig. 3). This range is chosen to exclude the data before the first minimum, where the separation magnitudes are low and thus challenging to fit. We use the `curve_fit` function in the open source scientific computation library `SciPy` [46] to perform the fitting. Once fit, we obtain the parameters λ_n and c, and the location of the crack tip is thus obtained at $\tilde{x} = c$ (red dot in Fig. 3). Beyond this point, the data can be compared to the second part of the function $\delta_n(x > 0)$ using the obtained parameters λ_n and c, with no additional fitting parameters.

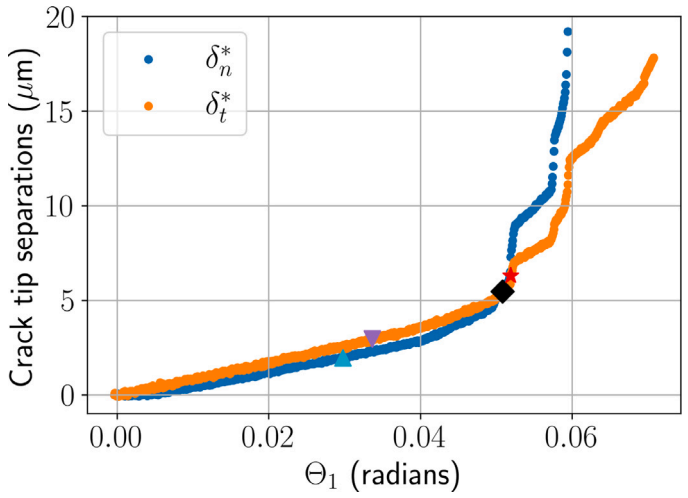

Fig. 4. Measured crack-tip separations versus end rotation under the mixed-mode condition, $\Theta_2/\Theta_1 = 0.5$. The symbols mark the points of damage initiation and onset of crack growth as determined in Fig. 6.

This process was repeated at different times for the same specimen and it was found that the crack tip could be estimated within ± 100 microns, which leads to an effective error in δ_n^* of about 13%. The corresponding k_n values for the parameter λ_n from the curve fitting across different specimens ranged from 4×10^{12} to 13×10^{12} Pa/m. However, it turns out that this range of interaction stiffness has very little effect on the initial slope of the moment–rotation response. This is consistent with the fact that the initial stiffness is of secondary importance in traction-separation relations [10,47]. Note that a similar approach was taken by [43] to determine the crack front location under displacement control, which requires three fitting parameters. Here, only two fitting parameters are required, owing to the self-similar separation profile under the rotation control.

For each of the mixed-mode experiments described later in the article, a preload in the linear regime was applied under Mode-I loading in order to first locate the crack front using the above procedure. The sample was then unloaded before the appropriate mode-mix was applied.

4. Data reduction for a representative case ($\Theta_2/\Theta_1 = 0.5$)

In this section, we present the results for a mixed-mode experiment conducted under rotation control with a prescribed ratio, $\Theta_2/\Theta_1 = 0.5$. The end-rotation of the upper beam (Fig. 2), Θ_1, is ramped at 0.01 degrees per second in all experiments. After the location of the initial crack tip was obtained, the normal and tangential components of the crack tip separations were measured using digital image correlation. However, the relative separations at the interface cannot be directly obtained from the images since classical digital image correlation is known to be inaccurate near boundaries [48]. We therefore measured the axial (u_1, u_2) and transverse (v_1, v_2) displacements and rotations (ϕ_1, ϕ_2) along the neutral axes of the two beams. Then, following the Euler–Bernoulli hypothesis for the deformation of the beams, the normal separation is simply $\delta_n = v_1 - v_2$, and the tangential separation of the interface is $\delta_t = u_1 - u_2 + \frac{h}{2}(\phi_1 + \phi_2)$. Thus, the interfacial separations were obtained using the digital image correlation data along the neutral axes, well-removed from any edges.

Fig. 4 shows the crack-tip separations measured as functions of the applied end rotation. Both the normal and shear separations initially increased linearly before departing from the linear response due to damage initiation at $\Theta_1 \approx 0.03$ radian. The separations increased more steeply as the crack begins to grow at $\Theta_1 \approx 0.05$ radian. It should be noted here that, at low end-rotation levels, the crack-tip separations are below the resolution of the digital image correlation measurements, which can manifest in the form of an apparent lag in the normal crack-tip separation in Fig. 4.

Fig. 5(a) shows the measured moment–rotation response for the far field gearing ratio of $\Theta_2/\Theta_1 = 0.5$. We notice that the torques first exhibit a linear behavior before developing damage (departing from linearity) and subsequent crack growth. The asymmetric loading can be decomposed into symmetric and anti-symmetric parts, with $M_d = (\mathcal{M}_1 - \mathcal{M}_2)/2$ and $M_s = (\mathcal{M}_1 + \mathcal{M}_2)/2$, respectively, as shown in Fig. 5(b). However, it is unclear from these data when damage initiation and crack growth occur. The symbols that denote these events are determined after processing the J-integral *vs.* crack tip separation responses (Fig. 6).

The two sets of data in Figs. 4 and 5(b) are used to generate the relations between the normal and tangential components of the J-integral and the corresponding crack-tip separations (Fig. 6). The components of J-integral are calculated according to Eq. (2). This calculation does not require the knowledge of the initial crack length. Then, by Eq. (1), the derivatives of the J-integral components with respect to the corresponding crack-tip separations generate the traction-separation relations at the initial crack tip. For small separations, the J-integral is expected to be quadratic, in accordance with the initially linear traction–separation relations. Once damage initiates, the tractions would decrease, corresponding to an inflection point of the J-integral in Fig. 6. Thus, this inflection

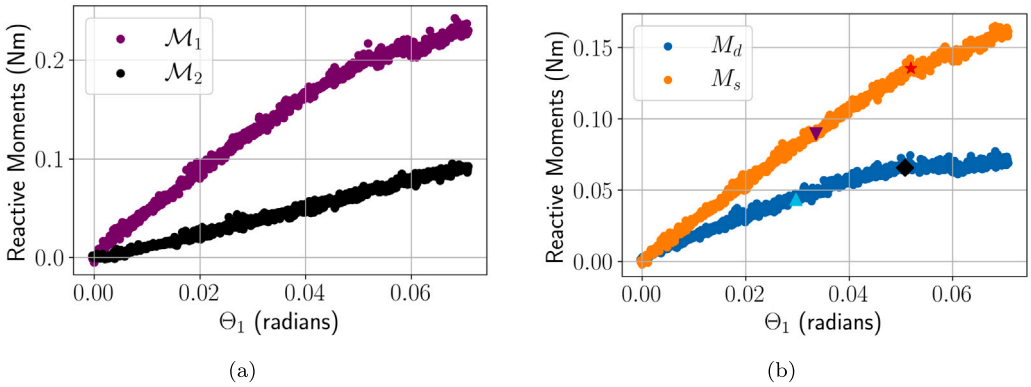

Fig. 5. Measured reactive moments versus end-rotation under the mixed-mode condition with $\Theta_2/\Theta_1 = 0.5$. (a) Reactive moments $\mathcal{M}_1$ and $\mathcal{M}_2$. (b) Mode-decomposed moments M_d and M_s. The symbols in (b) mark the points of damage initiation and onset of crack growth for each mode as determined in Fig. 6.

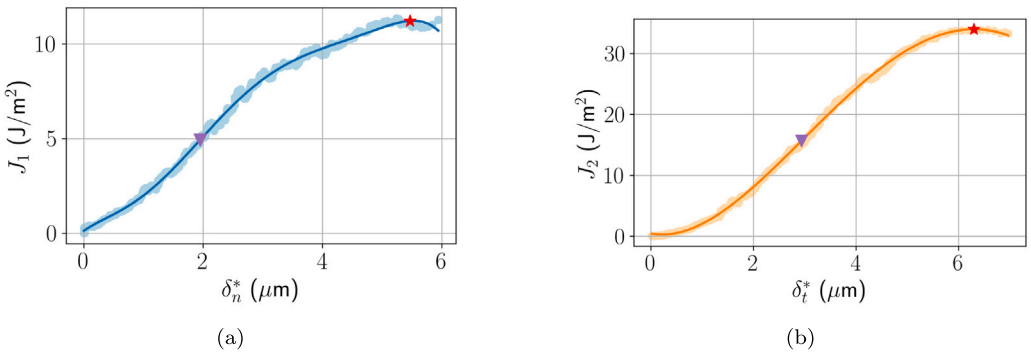

Fig. 6. Normal and shear components of the J-integral versus the corresponding crack-tip separations for $\Theta_2/\Theta_1 = 0.5$. The data are fitted with high-order polynomials to detect an inflection point as the point of damage initiation (marked by triangles). The peak of each J-integral component is marked (stars) as the onset of crack growth.

point could be used to determine the onset of damage, since manually locating the departure from linearity in Figs. 4 and 5 turned out to be subject to higher uncertainty. Accordingly, higher order polynomials were fit to the J-integral versus the crack-tip separation responses as shown in Fig. 6. Since we have assumed linear traction–separation relations prior to damage initiation, the goal of these fittings is to determine the inflection point for damage initiation and subsequently the traction-separation relations in the softening regime. Note that, if the two traction-separation relations for normal and shear interactions under the mixed-mode condition can be described by a single damage parameter, the point of damage initiation would have to be simultaneous for both components, and both tractions would drop to zero once the damage is fully developed at the same instant of time. However, no such constraint was placed on the fitting, thereby allowing for a validation of the above assumption. In particular, the two inflection points in Fig. 6 are marked correspondingly in Fig. 4 and Fig. 5b. It shows that damage initiation did not occur at the exactly same instant for the two modes. Moreover, the initiation of crack growth as determined by the zero slope in the J-integral response for each mode in Fig. 6 is also marked in Fig. 4 and Fig. 5(b). It shows that initiation of crack growth occurred nearly at the same instant ($\Theta_1 \approx 0.05$) for both modes.

The differentiation of the data (Fig. 6) resulted in the normal and shear traction-separation relations that are shown in Fig. 7. In addition to assuming an initially linear response for each traction–separation relation, the softening response was truncated whenever the derivatives of the J-integral became negative. Thus, the peak of each J-integral component is taken to be the critical value for crack growth under the mixed-mode condition. In this case, the two critical values are $\Gamma_1 \approx 11.3$ J/m^2 and $\Gamma_2 \approx 33.9$ J/m^2, which makes the total toughness $\Gamma = \Gamma_1 + \Gamma_2 \approx 45.2$ J/m^2 for $\Theta_2/\Theta_1 = 0.5$. The inflection points of the J-integrals in Fig. 6 correspond to the peak tractions in Fig. 7, as the normal and shear strength at 3.47 and 8.39 MPa, respectively. With the peak tractions and the corresponding separations, the initially linear responses are obtained with the initial stiffness values at 1.78×10^{12} and 2.85×10^{12} Pa/m for the normal and shear interactions, respectively. These values are slightly smaller than those that were determined for the interface between silicon and the same epoxy [31].

5. Results and discussion

Now that the process of extracting mixed-mode traction-separation relation has been established, we present the extracted traction-separation relations over a range of mode-mix with the applied rotation ratios, $-1 < \Theta_2/\Theta_1 < 0.8$. Values of $\Theta_2/\Theta_1 > 0.8$

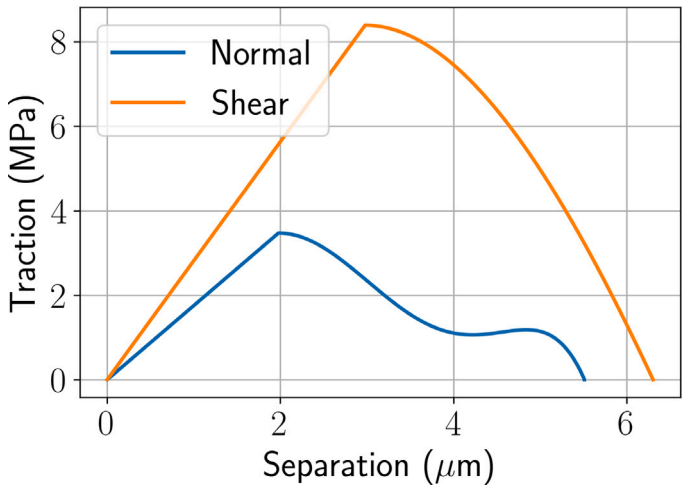

Fig. 7. Normal and shear traction–separation relations obtained from Fig. 6 for $\Theta_2/\Theta_1 = 0.5$.

were attempted but the torque levels that were required to cause delamination crack growth at the aluminum/epoxy interface considered here exceeded the current torque capacity of the loading device. The stage is set by first defining the measures of mode-mix considered here. This is followed by a presentation of the traction-separation relations and the associated properties (e.g., stiffness, strength, toughness). Discussions are made on the initiation and evolution of damage in a mixed-mode setting as well as various fracture paths.

5.1. Measures of the mode-mix

Although the symmetry of the specimen allowed the components of the J-integral to be separated [39], the traction–separation relations so obtained may themselves be coupled and mode-mix dependent. There are various measures of the mode-mix, but the two measures that are directly obtained in the experiments conducted herein are: (1) $\psi_J = \arctan\left(\sqrt{\frac{J_2}{J_1}}\right)$, based on the components of the J-integral, and (2) $\psi_\delta = \arctan\left(\frac{\delta_t^*}{\delta_n^*}\right)$ from the local measurements of the crack-tip separations.

In the linearly elastic regime, both δ_n^* and δ_t^* vary linearly with the applied end rotations, so that the ratio δ_t^*/δ_n^* remains constant for a constant Θ_2/Θ_1. Thus, the local mode-mix measured by ψ_δ remains constant in the linear regime. Similarly, the mode-mix measured by ψ_J also remains constant in the linear regime, as both J_1 and J_2 vary quadratically with the end rotations. However, the two measures of mode-mix are not necessarily equal unless the initial stiffness is the same for both the normal and shear interactions. Here, we use ψ_J as the nominal mode-mix. Once the damage initiates, however, the variations in the J-integrals and the crack-tip separations become more complicated, and the mode-mix by any measure could change as damage evolves.

Under the rotation control, the components of J-integral are directly related to the reactive moments by Eq. (2), so that $\psi_J = \arctan\left(\frac{\sqrt{3}}{2}\frac{M_s}{M_d}\right)$, which makes this a straight forward nominal measure of mode-mix for reference purposes. Given the low signal to noise ratio as loading begins, the mode-mix, being a ratio, oscillates significantly. The M_d and M_s data are therefore fit linearly in the region where their values is not so small as to be noise dominant but not as large as to depart from linearity, as defined by the inflection point approach. The results are tabulated in Table 1, which lists the five values of ψ_J that are considered here. They span a relatively wide range, from almost pure Mode I to about 75 degrees for a Mode II dominant mode-mix.

5.2. Traction–separation relations and fracture toughness

The traction-separation relations that were extracted at four other nominal mode-mix angles are presented in Fig. 8. Note that no tangential component of traction-separation relation was obtained in Fig. 8a, which is very close to pure Mode I ($\psi_J \approx 2°$). In this case, the tangential crack-tip separation was below the resolution and was therefore taken to be zero. In the linear regime, the normal stiffness values ranged from 1×10^{12} to 4×10^{12} Pa/m in no particular order (k_n in Table 1). Similarly, the initial stiffness for shear interactions ranged from 2.9×10^{12} to 4.5×10^{12} Pa/m. Such a range of stiffness values does not significantly affect the slope of the initial loading response of the specimen [31]. The subsequent softening portion of several traction-separation relations have small oscillations. This is because of the higher order polynomials that were used to fit the J-integral versus the crack-tip separations (δ_n^* and δ_t^*) data. They are needed to capture both the inflection point for damage initiation and the subsequent softening portion of these plots. Such oscillations may not represent the true traction–separation response of the interface, as the tractions are expected to monotonically decrease with the separations after damage initiation. Nonetheless, the current approach allows us to determine

Table 1
Critical parameters for the extracted traction-separation relations.

Θ_2/Θ_1	−1	0	0.4	0.5	0.8
ψ_J (Degrees)	2.34	27.00	53.32	57.39	74.84
Γ_1 (J/m^2)	18.3	13.2	11.50	11.23	4.38
Γ_2 (J/m^2)	NA	3.21	22.23	33.96	132.84
Γ (J/m^2)	18.3	16.41	33.73	45.19	137.22
σ_0 (MPa)	3.65	4.55	3.04	3.47	1.63
τ_0 (MPa)	NA	2.99	7.32	8.39	15.56
k_n ($\times 10^{12}$ Pa)	2.96	4.17	1.27	1.78	1.03
k_t ($\times 10^{12}$ Pa)	NA	4.46	2.97	2.85	3.36
δ_n^f (μm)	27.87	9.30	6.52	5.47	3.07
δ_t^f (μm)	NA	2.03	5.51	6.30	11.64

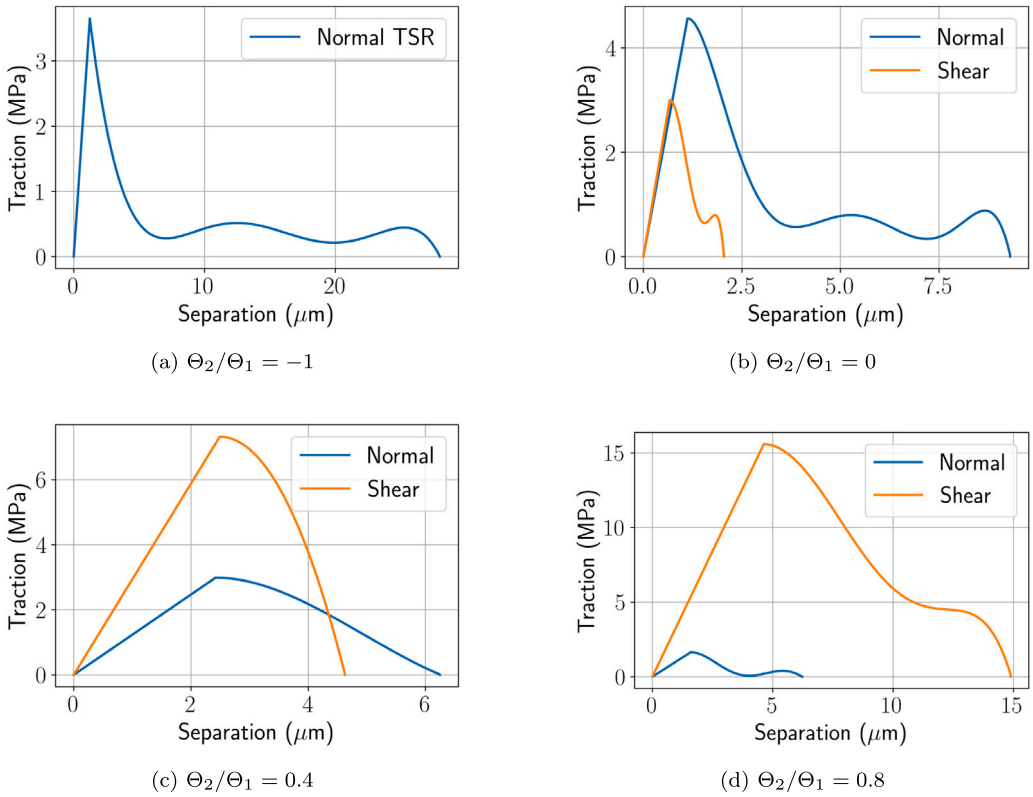

(a) $\Theta_2/\Theta_1 = -1$ (b) $\Theta_2/\Theta_1 = 0$

(c) $\Theta_2/\Theta_1 = 0.4$ (d) $\Theta_2/\Theta_1 = 0.8$

Fig. 8. Extracted traction-separation relations for different mode mix values.

the critical parameters (e.g., strength and toughness) and the approximate forms of the traction–separation relations under the mixed-mode conditions.

The overall fracture toughness, $\Gamma = \Gamma_1 + \Gamma_2$, was determined by examining the J-integral versus crack-tip separation responses by noting the peak values of J_1 and J_2 at the onset of crack growth. As plotted in Fig. 9(a), the fracture toughness increases with increasing mode-mix ψ_J. This trend is not necessarily universal but has been observed from some of the earliest studies on interfacial fracture [49–51]. The overall fracture toughness does not seem to change much at small ψ_J values for Mode I dominant cases, but increases sharply for mode-mix ψ_J above 45 degrees.

The mode-mix dependent interfacial toughness values are often fit with an expression [52],

$$\Gamma = \Gamma_0 \left[1 + (1 - \lambda)\tan^2 \psi\right]. \tag{4}$$

Taking $\psi = \psi_J$, Eq. (4) with the values of $\Gamma_0 = 19.58$ J/m^2 and $\lambda = 0.62$ provides a fit that was within two standard deviations to the data (Fig. 9(a)).

The individual contributions from the normal and shear interactions are brought out in Fig. 9(b). The data for Γ_1 and Γ_2 are obtained directly from the peak values of J-integral components based on the measured reactive moments. The values of Γ_1 and Γ_2 are listed in Table 1 for the five mode-mix values. The lines in Fig. 9(b) follow Eq. (4) by assuming that $\tan^2 \psi = \Gamma_2/\Gamma_1$, which leads

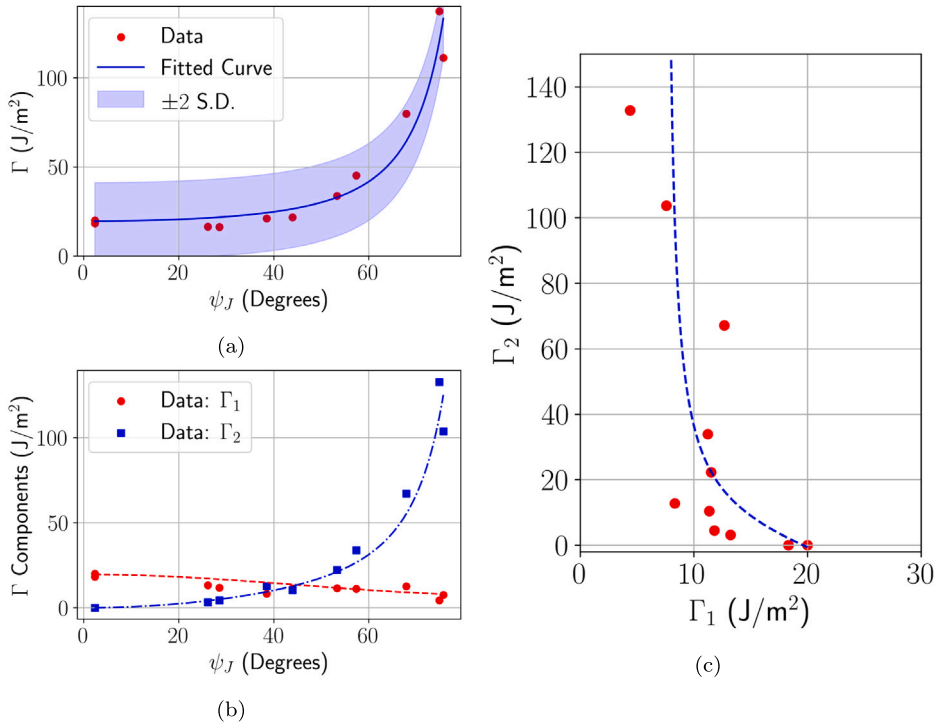

Fig. 9. (a) Overall fracture toughness as a function of the nominal mode-mix. The data is fitted using Eq. (4), and the shaded band shows ± 2 standard deviations of the fitting. (b) Individual fracture toughness components versus the nominal mode-mix, comparing the data with the predictions following the decomposition of Eq. (4). (c) Fracture envelope data and the theoretical prediction (dashed line).

to a decomposition of Γ: $\Gamma_1 = \frac{\Gamma(\psi)}{1+\tan^2\psi}$ and $\Gamma_2 = \frac{\Gamma(\psi)}{1+\cot^2\psi}$. Although the ratio Γ_2/Γ_1 in general is different from the ratio J_2/J_1 in the linear regime, the above decomposition of Eq. (4) appears to capture the data fairly well with no additional fitting parameters. The normal component of the toughness (Γ_1) decreases slowly as the mode-mix increases. On the other hand, the shear component Γ_2 increases strongly with mode-mix.

A fracture envelope can be constructed from the data in Fig. 9(b) and Eq. (4). Again, assuming $\tan^2\psi = \Gamma_2/\Gamma_1$, Eq. (4) predicts a fracture envelope in terms of the two components Γ_1 and Γ_2: $\Gamma_2 = \Gamma_1(\Gamma_0 - \Gamma_1)/(\Gamma_1 - (1-\lambda)\Gamma_0)$. It appears that the data roughly follows this envelope, as shown in Fig. 9(c). Note that the parameters Γ_0 and λ obtained earlier have been used here for the predicted envelope, and the data of Γ_1 and Γ_2 is from the mixed-mode experiments. The expression Eq. (4) predicts an unbounded toughness in pure Mode II as $\psi \to 90°$. The unbounded toughness has been justified in cases where asperity locking as a shielding mechanism is significant [53]. Moreover, Eq. (4) predicts a fracture envelope with a minimum value for Γ_1: $\min(\Gamma_1) = (1-\lambda)\Gamma_0$. This implies that fracture cannot occur if the normal component of J-integral is below a threshold. In other words, a minimum opening mode is required for fracture, consistent with the unbounded toughness in the limit of pure Mode II.

5.3. Damage initiation and strength

Next we focus our attention on damage initiation and the strength of the interface. It is typically assumed that the tractions at the interface first increase with the separation linearly prior to damage initiation. Upon damage initiation, the tractions decrease. Thus, the peak tractions for the normal and shear traction-separation relations are taken as the strengths, σ_0 and τ_0, and they are shown in Fig. 10 as functions of the mode-mix values. The strength values are also listed in Table 1 for the five cases. The shear strength typically increases with mode-mix, while the normal strength remains nearly constant. When $\psi_J \approx 0$, the shear traction is close to zero when the normal traction reaches the peak. As ψ_J increases, the increasing shear strength values have been fit with a function that saturates at a constant strength as $\psi_J \to 90°$. In typical cohesive zone models, the normal and shear strengths are taken to monotonically decrease and increase with increasing mode-mix, respectively, following a mixed-mode damage initiation criterion [54]. However, our experiments show that the normal strength is nearly constant for the range of mode-mix values considered here.

5.4. Damage evolution

In typical cohesive zone models, a single damage parameter is used to describe the softening part of the traction-separation relations: $\sigma = (1-D)k_n\delta_n$ and $\tau = (1-D)k_t\delta_t$, where the damage parameter D is a function of both separations, $D(\delta_n, \delta_t)$. Herein,

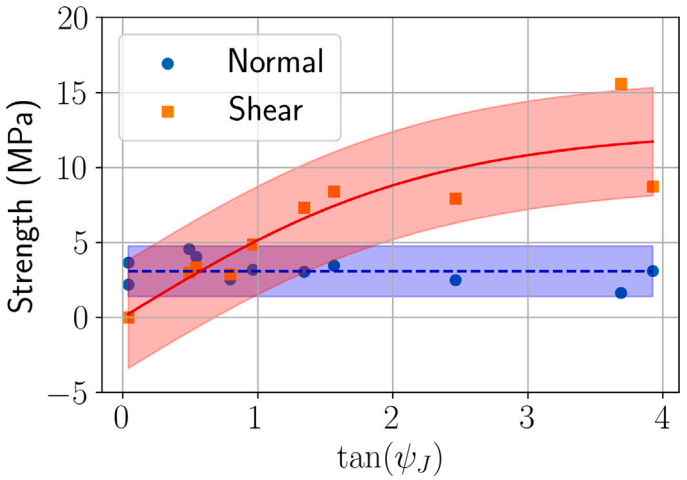

Fig. 10. Normal and shear strength values versus the nominal mode-mix, shown with a ±2 standard deviation bands. The shear strength data is fit by a function of the form $\tau_0 = a\tanh(b\tan\psi_J)$ with $a = 12.5$ MPa and $b = 0.44$ (solid line). The normal strength data is approximately constant, $\sigma_0 = 3$ MPa (dashed line).

since the normal and shear traction-separation relations have been developed separately for each mode-mix (Fig. 8), it stands to reason that it might be necessary to use two independent damage parameters instead of just one. Let the damage parameters be D_n and D_t for the normal and shear interactions, respectively. Both the damage parameters are zero prior to damage initiation and subsequently should monotonically increase with the respective separation to reach $D_n = D_t = 1$ for full damage or fracture. During damage evolution, the tractions are: $\sigma = (1 - D_n)k_n\delta_n$ and $\tau = (1 - D_t)k_t\delta_t$. The extracted traction-separation relations can therefore be used to determine the damage parameters as $D_n = 1 - \frac{\sigma}{k_n\delta_n}$ and $D_t = 1 - \frac{\tau}{k_t\delta_t}$. Fig. 11 shows the evolution of the two damage parameters for the five mode-mixes corresponding to the traction-separation relations in Figs. 7 and 8. Each damage parameter is shown as a function of the corresponding separation, that is, $D_n(\delta_n)$ and $D_t(\delta_t)$ with the understanding that $D_n(\delta_n)$ will assume a functional form dependent on the value of δ_t, and the same is true for $D_t(\delta_t)$.

The effect of damage evolution on the mode-mix solicits some comments: the normal damage (Fig. 11(a)), D_n, seems less likely to be affected by the mode-mix than the tangential damage (Fig. 11(b)). The crack tip opening values at damage initiation (δ_n^i) may essentially be assumed to be constant and the subsequent damage evolution is largely similar, within the measurement uncertainty. On the other hand, the values of crack tip shear separation at damage initiation (δ_t^i) increase notably with the mode-mix and are also distributed much more widely. If this is indeed the case, then the normal interaction is independent of shear, and the shear interaction depends on the normal interaction due to the presence of other mechanisms such as friction. More experiments are needed to address this hypothesis.

Moreover, if we consider the variation of D_t with D_n (Fig. 12), it can be seen that none of the responses follow the diagonal path that corresponds to a single damage parameter. It is also clear that the damage does not start simultaneously in the normal and shear interactions. In the Mode I dominant cases, the damage in the normal direction starts earlier than that in the tangential direction, while the opposite is true for the Mode II dominant cases. This also enforces our hypothesis of δ_n^i being constant and δ_t^i increasing with the mode-mix. Also worthy of note is the fact that the two damage parameters reach one (full damage) at about the same time for most cases. This is a consequence of the data for J-integral versus the crack-tip separations (δ_n^* and δ_t^*), where both components of the J-integral reach the peak value at approximately the same time (or Θ_1) due to the onset of crack growth. The slight differences are likely due to the chosen functions fitting the data but not necessarily reaching the peak at the same point in time. In addition, the non-monotonicity in the damage evolution is lent by the traction-separation relations themselves and is a result of the higher order polynomial fitting and possibly some noise in the data, as explained earlier.

5.5. Fracture paths and comments on inverse extraction

Compared to displacement control, rotation control has been considered herein for its expected relatively small change in mode-mix as damage develops and crack growth ensues [35]. Thus it is instructive at this stage to track the paths that are taken in $J_1 - J_2$ and $\delta_n^* - \delta_t^*$ spaces, particularly as damage develops. While the components of J-integral define the nominal or global mode-mix ψ_J, the normal and tangential separations at the initial crack tip, δ_n^* and δ_t^*, define the local mode-mix ψ_δ. The paths taken in the $J_1 - J_2$ space (Fig. 13) are largely radial, even after damage initiation. As shown in Fig. 9(c), the fracture envelop takes an unusual shape (dashed line), as opposed to the commonly assumed linear or elliptical envelopes. Note that the fracture envelope developed here was generated by prescribing nominally radial/proportional loading paths. One of the strengths of the dual actuator devices is that different loading paths in the $J_1 - J_2$ space may be probed, potentially resulting in path-dependent fracture envelopes. Efforts in this direction are already underway.

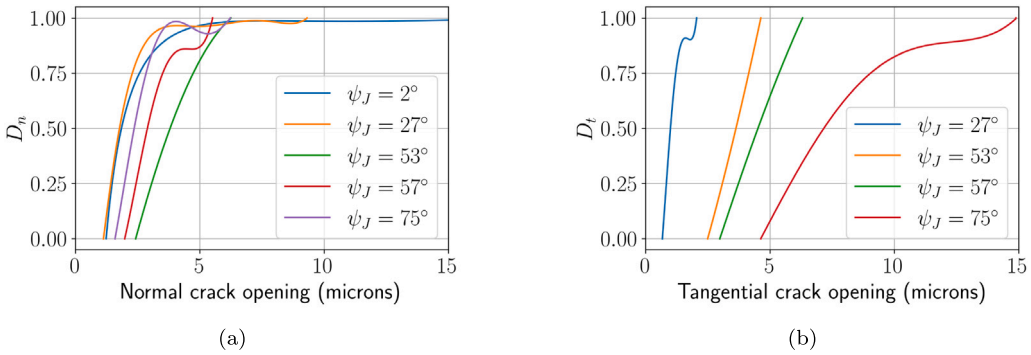

Fig. 11. Damage parameters versus the respective crack-tip separations.

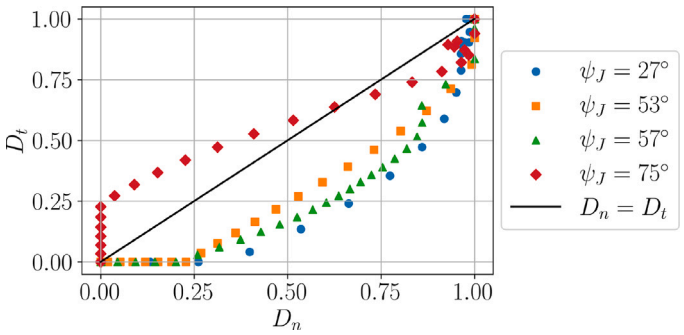

Fig. 12. The evolution of normal and shear damage parameters as opposed to using a single damage parameter.

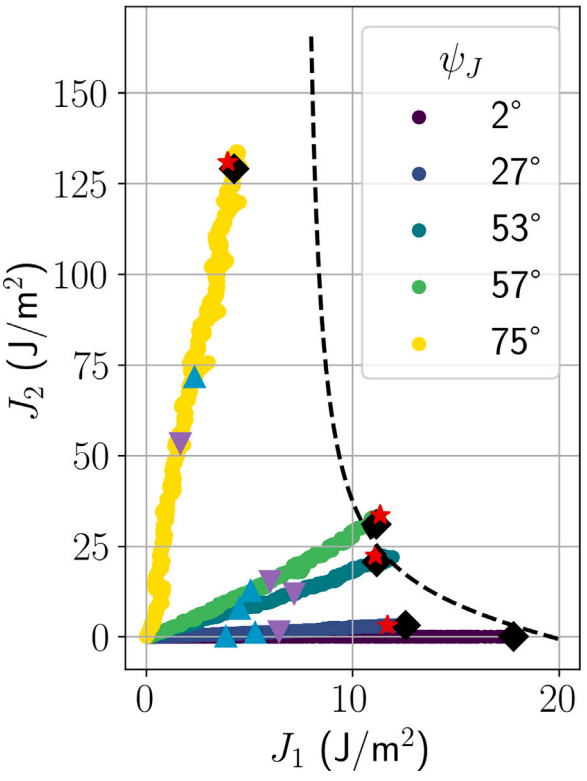

Fig. 13. Fracture paths in the $J_1 - J_2$ space. Cyan (normal) and purple (tangential) triangles mark the points of damage initiation, while black diamonds (normal) and red stars (tangential) mark fracture. The dashed line show the fracture envelope based on Eq. (4).

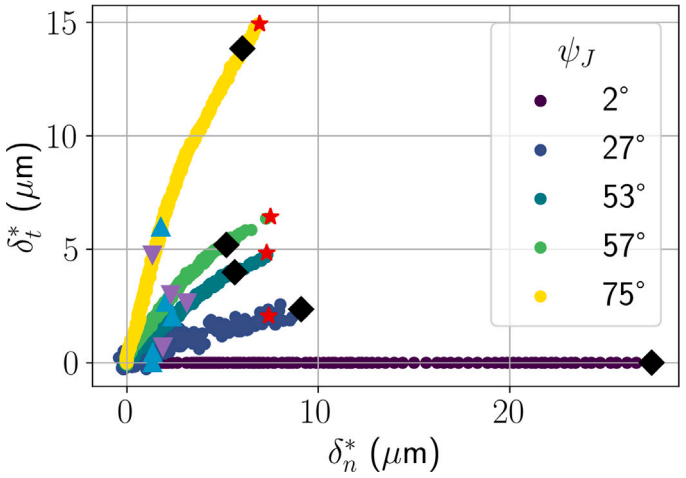

Fig. 14. Fracture paths in the $\delta_n^* - \delta_t^*$ space. Cyan (normal) and purple (tangential) triangles mark the points of damage initiation, while black diamonds (normal) and red stars (tangential) mark fracture.

The paths taken in the $\delta_n^* - \delta_t^*$ space (Fig. 14) exhibited more departure from radial ones. The paths prior to damage initiations are close to radial, where the local mode-mix ψ_δ remains constant. It appears that the values of δ_n^i are essentially independent of mode-mix as noted earlier, and as seen through damage initiation in both normal and shear direction. However, following damage initiation, the paths are notably nonlinear, except for the case of nearly Mode-I ($\psi_J = 2°$). As the damage develops under mixed-mode conditions, the local mode-mix (ψ_δ) decreases noticeably. At this stage, the data does not provide a clear fracture envelope governing the range of interaction (δ_n^f, δ_t^f), although the values of δ_t^f occur at approximately the same value of δ_n.

Nonetheless, the overarching message conveyed through our results is the need of modeling approaches that can capture the mixed-mode traction-separation relations. The cohesive zone models implemented in ABAQUS [55] assume that the normal and shear traction degradation depends on a single damage parameter, based on the work of Camanho & Davila [54]. Although this might seem convenient, it fails to capture the data presented in Fig. 12, where two damage parameters are needed to describe the degradation of normal and shear tractions separately. Such a model stands a better chance of representing mixed-mode traction-separation relations.

We end this discussion by highlighting some of the advantages and disadvantages of this rotation control device. As in any novel device, significant development of the basic concept was required in order to provide meaningful results. The initial goal of minimizing the variation of the nominal mode-mix with crack length was achieved (Fig. 13). Nonetheless, the local mode-mix decreased as the damage developed (Fig. 14). Of course some of this change in mode-mix is inherent to configurations where laminated beam geometries are involved. Nonetheless, another component of the change in mode-mix could be related to the damage evolution process itself. The only configurations that allow the latter effect to be tracked directly are bi-axially loaded bi-material strips [56–58].

Testing specimens with brittle adherends under rotation control is a bigger challenge than in a displacement control setting. The uniform bending under rotation control results in the entire top and bottom near surface volumes of the cracked portion of the specimen being probed by the same level of high stress, which makes encountering a critical flaw in an adherend more likely. However, even under displacement control, similar problems, albeit to a lesser extent, were encountered with Si/Epoxy/Si samples [31]. This is one reason why the Al/epoxy/Al specimens were considered for initial proof of concept purposes. However, it seems that this particular interface is subject to more variability. The relatively very long cohesive zones encountered here may also induce the possibility of interface switching during crack propagation. Nonetheless, cohesive failure of the epoxy was not seen. Testing of interfaces between more brittle materials, such as silicon, may be conducted by reinforcing the beams.

The onset of crack growth is much easier to detect in displacement control, due to the peak that occurs in the load–displacement response. This is true for interfaces whose toughness is independent or dependent of the mode-mix. Under rotation control, for an interface that toughens with mode-mix, the torque increases continuously as the crack grows [35], making the onset of crack growth more difficult to discern from the torque-rotation response. The crack tip separation responses are more discriminating but not directly accessible in the current configuration where they are obtained following a substantial amount of post processing. The servomotors were used at the lowest allowable rate of 0.01 degrees per second in order to account for challenges for the servo motor control that were related to the fidelity of feedback control that is inherent in such motors. A balance had to be struck that resulted in a small lag in the rotations that were applied by the primary and the secondary motor. One interesting feature of the rotation control setup that is worthy of note is that how the whole extraction process is agnostic to the crack length or the total length of the sample. The only quantity needed is the location of the crack tip. This self-similarity property adds to the list of advantages the rotation control offers.

6. Conclusions

This work confirms that dual actuators and rotation control both provide unique and favorable characteristics for the direct extraction of traction-separation relations. A novel dual actuator device that controls the end rotations of cracked laminated beam specimens in order to prescribe any mode-mix is developed. Exemplar specimens consisting of aluminum strips bonded by an epoxy were employed in this study as the ductile nature of the aluminum minimized concerns regarding adherend cracking prior to delamination. Torque cells measured the reactive moments while digital image correlation was used to determine the beam displacements near the initial crack front as the end rotations were being independently controlled. The displacement measurements were used to determine the location of the initial crack front in these opaque specimens. Rotation control simplifies the technique [43] developed for specimens loaded under displacement control. Once the crack front is located, the normal and tangential components of crack-tip separations are then directly extracted from digital image correlation. The measurements of reactive torques provide the normal and shear components of the J-integral, which are separable due to the symmetry of the specimen [39]. Differentiation of each component of the J-integral with respect to its associated crack-tip separation component then provides the normal and shear components of the traction-separation relation at any particular mode-mix. Note that although the extraction is decoupled, the traction-separation relations in the two directions are generally coupled and thus depend on the mode-mix.

A series of normal and tangential traction-separation relations were extracted over a wide range of mode-mix phase angles and were clearly a function of mode-mix. The toughness of the aluminum/epoxy interface increased with increasing shear. For this particular interface, the mixed-mode fracture envelope did not follow the linear coupling between the normal and shear components of the J-integral that is commonly assumed. The initiation and development of damage were also tracked as a function of the mode-mix. Over the range of mode-mixes that were considered, the resulting normal strength was independent of mode-mix while the shear strength increased. While the higher order fits were useful in determining strength, they did not always capture the expected initially quadratic response. As a result, the stiffness of the interactions was simply taken to be constant until the strength was achieved. On the other hand, the derivatives of the higher order polynomials did provide the softening response of the traction-separation relations. The damage development was tracked by comparing the unloading stiffness at any point in the softening response to the initial stiffness of the traction-separation relations. The completion of damage development in the normal and shear interactions occurred nearly simultaneously at all mode-mixes. However, under Mode I dominant conditions, damage initiation in the normal interaction occurred earlier than its shear counterpart. The situation was reversed in the shear dominant cases, making it clear that two, rather than one, damage parameters are required in order to track damage evolution in mixed-mode delamination. In addition, the nominal mode-mix did not change appreciably as the damage evolved. However, the drop in the local mode-mix was much more apparent when crack tip separations were tracked.

The dual actuator device operating in rotation control on symmetric laminated beam specimens has facilitated the simultaneous extraction of the normal and tangential components of the traction-separation relations at any mode-mix. This in turn has allowed some commonly assumed criteria for damage initiation and completion to be critically assessed, at least for the aluminum/epoxy interface considered here. Nonetheless, the approach that has been taken here can be extended to other interfaces in order to determine how general some of the observations that have been made herein actually are.

CRediT authorship contribution statement

Mohammad A. Ansari: Writing – review & editing, Writing – original draft, Visualization, Validation, Software, Methodology, Investigation, Formal analysis, Data curation, Conceptualization. **Rujing Zha:** Writing – review & editing, Methodology, Conceptualization. **Rui Huang:** Writing – review & editing, Writing – original draft, Visualization, Validation, Supervision, Resources, Methodology, Investigation, Funding acquisition, Formal analysis, Conceptualization. **Kenneth M. Liechti:** Writing – review & editing, Writing – original draft, Visualization, Validation, Supervision, Resources, Project administration, Methodology, Investigation, Funding acquisition, Formal analysis, Data curation, Conceptualization.

Declaration of competing interest

The authors declare the following financial interests/personal relationships which may be considered as potential competing interests: This paper has not been submitted elsewhere

Acknowledgments

The authors gratefully acknowledge support from the Semiconductor Research Corporation, United States under Project Number 2023-PK-3183OSP.

Data availability

Data will be made available on request.

References

[1] Barenblatt GI. The formation of equilibrium cracks during brittle fracture. General ideas and hypotheses. Axially-symmetric cracks. J Appl Math Mech 1959;23(3):622–36.
[2] Dugdale DS. Yielding of steel sheets containing slits. J Mech Phys Solids 1960;8(2):100–4.
[3] Sills R, Thouless M. The effect of cohesive-law parameters on mixed-mode fracture. Eng Fract Mech 2013;109:353–68.
[4] Goutianos S, Sørensen B, Thouless M. Mixed-mode cohesive laws and the use of linear-elastic fracture mechanics. Eng Fract Mech 2021;252:107792.
[5] Wei Y. A stochastic description on the traction-separation law of an interface with non-covalent bonding. J Mech Phys Solids 2014;70:227–41.
[6] Estevez R, Tijssens M, Van der Giessen E. Modeling of the competition between shear yielding and crazing in glassy polymers. J Mech Phys Solids 2000;48(12):2585–617.
[7] Farmand-Ashtiani E, Alanis D, Cugnoni J, Botsis J. Delamination in cross-ply laminates: Identification of traction–separation relations and cohesive zone modeling. Compos Sci Technol 2015;119:85–92.
[8] Mohammed I, Liechti KM. Cohesive zone modeling of crack nucleation at bimaterial corners. J Mech Phys Solids 2000;48(4):735–64.
[9] Thouless M, Goutianos S. Cohesive-zone models and singularities at corners and cracks in homogeneous materials. J Mech Phys Solids 2023;171:105159.
[10] Gowrishankar S, Mei H, Liechti KM, Huang R. A comparison of direct and iterative methods for determining traction-separation relations. Int J Fract 2012;177:109–28.
[11] Sørensen BF, Jørgensen K, Jacobsen TK, Østergaard RC. DCB-specimen loaded with uneven bending moments. Int J Fract 2006;141:163–76.
[12] Sørensen BF, Jacobsen TK. Characterizing delamination of fibre composites by mixed mode cohesive laws. Compos Sci Technol 2009;69(3–4):445–56.
[13] Cox B, Marshall D. The determination of crack bridging forces. Int J Fract 1991;49:159–76.
[14] Li S, Thouless M, Waas A, Schroeder J, Zavattieri P. Use of a cohesive-zone model to analyze the fracture of a fiber-reinforced polymer–matrix composite. Compos Sci Technol 2005;65(3–4):537–49.
[15] Hong S, Kim K-S. Extraction of cohesive-zone laws from elastic far-fields of a cohesive crack tip: a field projection method. J Mech Phys Solids 2003;51(7):1267–86.
[16] Taira K, Colonius T. The immersed boundary method: a projection approach. J Comput Phys 2007;225(2):2118–37.
[17] Hong S, Chew HB, Kim K-S. Cohesive-zone laws for void growth—I. Experimental field projection of crack-tip crazing in glassy polymers. J Mech Phys Solids 2009;57(8):1357–73.
[18] Chew HB, Hong S, Kim K-S. Cohesive zone laws for void growth—II. Numerical field projection of elasto-plastic fracture processes with vapor pressure. J Mech Phys Solids 2009;57(8):1374–90.
[19] Kim H-G, Chew HB, Kim K-S. Inverse extraction of cohesive zone laws by field projection method using numerical auxiliary fields. Internat J Numer Methods Engrg 2012;91(5):516–30.
[20] Rokoš O, Peerlings R, Hoefnagels J, Geers M. Integrated digital image correlation for micro-mechanical parameter identification in multiscale experiments. Int J Solids Struct 2023;267:112130.
[21] Wei C, Zhang J, Liechti KM, Wu C. Deep-green inversion to extract traction-separation relations at material interfaces. Int J Solids Struct 2022;250:111698.
[22] Tran H, Gao Y, Chew H. Numerical and experimental crack-tip cohesive zone laws with physics-informed neural networks. J Mech Phys Solids 2024;193:105866.
[23] Alfano M, Furgiuele F, Leonardi A, Maletta C, Paulino G. Mode I fracture of adhesive joints using tailored cohesive zone models. Int J Fract 2009;157:193–204.
[24] Kim Y-R. Cohesive zone model to predict fracture in bituminous materials and asphaltic pavements: state-of-the-art review. Int J Pavement Eng 2011;12(4):343–56.
[25] Mello AW, Liechti KM. The effect of self-assembled monolayers on interfacial fracture. 2006.
[26] Cao Z, Tao L, Akinwande D, Huang R, Liechti KM. Mixed-mode traction-separation relations between graphene and copper by blister tests. Int J Solids Struct 2016;84:147–59.
[27] De Morais A. Novel cohesive beam model for the end-notched flexure (ENF) specimen. Eng Fract Mech 2011;78(17):3017–29.
[28] Kolluri M, Hoefnagels J, Van Dommelen J, Geers M. An improved miniature mixed-mode delamination setup for in situ microscopic interface failure analyses. J Phys D: Appl Phys 2010;44(3):034005.
[29] Bennati S, Fisicaro P, Valvo PS. An enhanced beam-theory model of the mixed-mode bending (MMB) test—Part I: Literature review and mechanical model. Meccanica 2013;48:443–62.
[30] Bennati S, Fisicaro P, Valvo PS. An enhanced beam-theory model of the mixed-mode bending (MMB) test—Part II: Applications and results. Meccanica 2013;48:465–84.
[31] Yang T, Gandhi V, Huang R, Liechti KM. Rate dependent fracture along a silicon/epoxy interface under mixed-mode loading conditions. Int J Solids Struct 2022;257:111129.
[32] Davidson BD, Sediles FO. Mixed-mode I–II–III delamination toughness determination via a shear–torsion-bending test. Compos Part A Appl Sci Manuf 2011;42(6):589–603.
[33] Singh HK, Chakraborty A, Frazier CE, Dillard DA. Mixed mode fracture testing of adhesively bonded wood specimens using a dual actuator load frame in Holzforschung, Vol. 64. Berlin, New York: Copyright by Walter de Gruyter; 2010, p. 353–61. http://dx.doi.org/10.1515/HF.2010.041.
[34] Pappas GA, Botsis J. Variations on R-curves and traction-separation relations in DCB specimens loaded under end opening forces or pure moments. Int J Solids Struct 2020;191:42–55.
[35] Ansari MA, Huang R, Liechti KM. Optimal dual actuator loading configurations for extracting mixed-mode cohesive relations from interacting beams. Int J Solids Struct 2023;270:112229.
[36] Gorman J, Thouless M. The use of digital-image correlation to investigate the cohesive zone in a double-cantilever beam, with comparisons to numerical and analytical models. J Mech Phys Solids 2019;123:315–31.
[37] Bao G, Suo Z. Remarks on crack-bridging concepts. 1992.
[38] Sørensen BF, Jacobsen TK. Determination of cohesive laws by the J integral approach. Eng Fract Mech 2003;70(14):1841–58.
[39] Wu C, Huang R, Liechti KM. Simultaneous extraction of tensile and shear interactions at interfaces. J Mech Phys Solids 2019;125:225–54.
[40] Yang T, Liechti KM, Huang R. A multiscale cohesive zone model for rate-dependent fracture of interfaces. J Mech Phys Solids 2020;145:104142.
[41] Turon A, Camanho P, Costa J, Renart J. Accurate simulation of delamination growth under mixed-mode loading using cohesive elements: Definition of interlaminar strengths and elastic stiffness. Compos Struct 2010;92(8):1857–64.
[42] Rajan S, Sutton MA, Fuerte R, Kidane A. Traction-separation relationship for polymer-modified bitumen under mode I loading: Double cantilever beam experiment with stereo digital image correlation. Eng Fract Mech 2018;187:404–21.
[43] Sun F, Blackman BR. Using digital image correlation to automate the measurement of crack length and fracture energy in the mode I testing of structural adhesive joints. Eng Fract Mech 2021;255:107957.
[44] Kanninen MF. An augmented double cantilever beam model for studying crack propagation and arrest. Int J Fract 1973;9:83–92.
[45] Williams J, Hadavinia H. Analytical solutions for cohesive zone models. J Mech Phys Solids 2002;50(4):809–25.

[46] Virtanen P, Gommers R, Oliphant TE, Haberland M, Reddy T, Cournapeau D, et al. SciPy 1.0: Fundamental Algorithms for Scientific Computing in Python. Nature Methods 2020;17:261–72. http://dx.doi.org/10.1038/s41592-019-0686-2.
[47] Tvergaard V, Hutchinson JW. The relation between crack growth resistance and fracture process parameters in elastic-plastic solids. J Mech Phys Solids 1992;40(6):1377–97.
[48] Sutton M, Matta F, Rizos D, Ghorbani R, Rajan S, Mollenhauer D, et al. Recent progress in digital image correlation: background and developments since the 2013 WM Murray Lecture. Exp Mech 2017;57:1–30.
[49] Cao H, Evans A. An experimental study of the fracture resistance of bimaterial interfaces. Mech Mater 1989;7(4):295–304.
[50] Wang J-S, Suo Z. Experimental determination of interfacial toughness curves using Brazil-nut-sandwiches. Acta Met et Mater 1990;38(7):1279–90.
[51] Liechti K, Chai Y. Asymmetric shielding in interfacial fracture under in-plane shear. 1992.
[52] Hutchinson JW, Suo Z. Mixed mode cracking in layered materials. Adv Appl Mech 1991;29:63–191.
[53] Evans AG, Hutchinson JW. Effects of non-planarity on the mixed mode fracture resistance of bimaterial interfaces. Acta Metall 1989;37(3):909–16.
[54] Camanho PP, Dávila CG. Mixed-mode decohesion finite elements for the simulation of delamination in composite materials. Technical report, 2002.
[55] Systèmes D. Abaqus/standard user's manual, version 2024. Providence, RI, USA: Dassault Systèmes; 2024.
[56] Liechti K, Knauss W. Crack propagation at material interfaces: I. Experimental technique to determine crack profiles. Exp Mech 1982;22:262–9.
[57] Liechti K, Chai Y-S. Biaxial loading experiments for determining interfacial fracture toughness. J Appl Mech 1991;58:680–7.
[58] Mello A, Liechti K. A piezoelectric biaxial loading device for interfacial fracture experiments. Exp Mech 2004;44:495–501.